



Cross sections of the $^{40}\text{Ca}(n, \alpha_0)^{37}\text{Ar}$ and $^{40}\text{Ca}(n, \alpha)^{37}\text{Ar}$ reactions in the 8.50–9.50 MeV neutron energy range

Jie Liu,¹ Haoyu jiang,¹ Zengqi Cui,¹ Yiwei Hu,¹ Haofan Bai,¹ Jinxiang Chen,¹ Guohui Zhang ,^{1,*}

Yu. M. Gledenov ,² E. Sansarbayar ,² G. Khuukhenkhuu,³ N. Battsooj ,³ L. Krupa ,^{4,5}

I. Chuprakov ,^{2,6,7} Xichao Ruan,⁸ Hanxiong Huang,⁸ Jie Ren,⁸ and Qiwen Fan⁸

¹State Key Laboratory of Nuclear Physics and Technology, Institute of Heavy Ion Physics, School of Physics, Peking University, Beijing 100871, China

²Frank Laboratory of Neutron Physics, Joint Institute for Nuclear Research, Dubna 141980, Russia

³Nuclear Research Centre, National University of Mongolia, Ulaanbaatar, Mongolia

⁴Flerov Laboratory of Nuclear Reactions, Joint Institute for Nuclear Research, Dubna 141980, Russia

⁵Institute of Experimental and Applied Physics, Czech Technical University in Prague, Horska 3a/22, Prague 2, 12800, Czech Republic

⁶L. N. Gumilyov Eurasian National University, Nur-sultan 010000, Kazakhstan

⁷The Institute of Nuclear Physics, Ministry of Energy of the Republic of Kazakhstan, Almaty 050032, Kazakhstan

⁸China Institute of Atomic Energy, Beijing 102413, China



(Received 23 July 2022; revised 20 September 2022; accepted 8 November 2022; published 28 November 2022)

Cross sections of the $^{40}\text{Ca}(n, \alpha_0)^{37}\text{Ar}$ and $^{40}\text{Ca}(n, \alpha)^{37}\text{Ar}$ reactions at five neutron energy points in the 8.50–9.50 MeV energy region were measured. The monoenergetic neutrons were produced through the $^2\text{H}(d, n)^3\text{He}$ reaction based on the HI-13 tandem accelerator of China Institute of Atomic Energy (CIAE). A twin gridded ionization chamber (GIC) was used as the charged particle detector. Detailed simulations were performed to determine the nuclear reaction events and detection efficiencies. Present results are compared with existing measurement and evaluation data, which shows that the evaluation data from all libraries are higher than the measurement data in the 8.50–9.50 MeV region for the $^{40}\text{Ca}(n, \alpha)^{37}\text{Ar}$ reaction. TALYS-1.9 code was used for theoretical calculations. Calculation results using the TALYS-1.9 code with the adjusted parameters are in agreement with the present measurements, which also show that the compound mechanism predominates the $^{40}\text{Ca}(n, \alpha)^{37}\text{Ar}$ reaction in the 8.50–9.50 MeV region. Both present measured forward/backward ratios and TALYS-1.9 calculations suggest that the direct and preequilibrium mechanisms are non-negligible for the $^{40}\text{Ca}(n, \alpha)^{37}\text{Ar}$ reaction in the 8.50–9.50 MeV region.

DOI: [10.1103/PhysRevC.106.054610](https://doi.org/10.1103/PhysRevC.106.054610)

I. INTRODUCTION

Calcium is one of the most widespread elements in nature as well as in the human body. ^{40}Ca is a double-magic nucleus with the abundance reaching up to 96.94%. The cross section of the $^{40}\text{Ca}(n, \alpha)^{37}\text{Ar}$ reaction is of interest for both nuclear physics theories and nuclear technology applications. Accurate and systematic cross sections enable us to test and improve the validity of different nuclear reaction models used in theoretical calculations [1]. The accurate cross sections for the $^{40}\text{Ca}(n, \alpha)^{37}\text{Ar}$ reaction, in which both α particles and ^{37}Ar nuclei are noble gas isotopes, is also important for applications in nuclear engineering, geology, and environment. In nuclear engineering, the $^{40}\text{Ca}(n, \alpha)^{37}\text{Ar}$ reaction is one of the sources of ^{37}Ar in the nuclear reactor gas effluents, which takes place on the calcium impurity present in reactor materials [2]. The radiation damage of the concrete shielding materials can be estimated with the cross section of the $^{40}\text{Ca}(n, \alpha)^{37}\text{Ar}$ reaction [2]. In geology and environment, the production of ^{37}Ar from the $^{40}\text{Ca}(n, \alpha)^{37}\text{Ar}$ reaction is also

of interest in lunar and geochemical studies, since gaseous products from the soil will be released into the atmosphere [3]. Furthermore, the on-site inspections for Comprehensive Nuclear-Test-Ban Treaty monitoring can be performed using the $^{40}\text{Ca}(n, \alpha)^{37}\text{Ar}$ reaction [4].

The $^{40}\text{Ca}(n, \alpha)^{37}\text{Ar}$ reaction has been measured for more than 50 years. However, existing experimental data is still insufficient. Four measurements [2,3,5,6] exist in EXFOR library [7] in the MeV neutron energy region since 1970. In the 1–6 MeV neutron energy region, the results of three existing measurements [3,5,6] are consistent within uncertainties. The evaluation data of this reaction in different libraries such as ENDF/B-VIII.0 [8], JENDL-5 [9], JEFF-3.3 [10], CENDL-3.2 [11], and TENDL-2019 [12] are in agreement in this region. In the 6–13 MeV neutron energy region, however, there is only one measurement. As a result, large deviations exist among different libraries. In the 13–15 MeV neutron energy region, there are two measurements that agree each other within the uncertainties [2,3] while the deviations in the evaluation data are reduced. Hence, accurate and systematic measurements and analysis for the $^{40}\text{Ca}(n, \alpha)^{37}\text{Ar}$ reaction are demanded especially in the 6–13 MeV region.

*Corresponding author: guohuizhang@pku.edu.cn

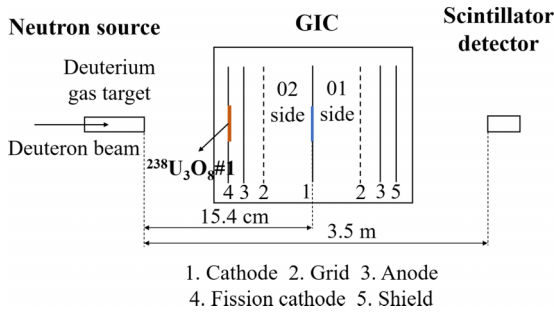


FIG. 1. Scheme of the experimental setup.

In the present work, cross sections of the $^{40}\text{E}(n, \alpha_0)$ and $^{40}\text{Ca}(n, \alpha)$ reactions were measured at five energy points in the 8.50–9.50 MeV neutron energy region using a twin gridded ionization chamber (GIC) and two back-to-back CaO samples. The details of experiments are illustrated in Sec. II. The data analysis is presented in Sec. III. The experimental results are displayed in Sec. IV. Theoretical analysis and discussions are illustrated in Sec. V, and the conclusions are drawn in Sec. VI.

II. EXPERIMENTS

The experiments were performed on the HI-13 tandem accelerator at China Institute of Atomic Energy (CIAE). Figure 1 is the scheme of the experimental setup, which includes three parts: the neutron source, the twin gridded ionization chamber (GIC) as the charged particle detector, and the EJ-309 liquid scintillator as the neutron detector.

Monoenergetic neutrons were produced through the $^2\text{H}(d, n)^3\text{He}$ reaction with a deuterium gas target. The gas cell was 3.0 cm in length and 1.0 cm in diameter and the pressure of the deuterium gas was ≈ 3.0 atm during measurements. A molybdenum foil 10.0 μm in thickness was used to separate the vacuum tube of the accelerator from the gas target. The kinetic energies of the deuterons were set from 6.00–7.00 MeV to obtain the monoenergetic neutrons from 8.50–9.50 MeV.

A twin GIC was used as the charged particle detector. The structure and the electronics of the GIC were described in Ref. [13]. The working gas of the GIC was Xe + 6.0% H_2 with the pressure of 1.095 atm in the present work. The distances of cathode grid and anode grid were 60.35 mm and 15.24 mm, respectively. The high voltages applied on the cathode and anodes were -1500 V and 750 V, respectively, and the grid electrodes were grounded.

As shown in Fig. 1, a ^{238}U sample ($^{238}\text{U}_3\text{O}_8\#1$) was glued on the shield of the GIC close to the neutron source (as the fission cathode) to monitor the relative neutron fluence. A sample changer with five sample positions was installed at the common cathode of the GIC, on which back-to-back double samples were placed as presented in Table I. Different kinds of samples were measured separately. The 01 side and 02 side of the GIC were measured simultaneously corresponding to the forward (0° – 90°) and backward (90° – 180°) events. The data of the samples is presented in Table II. The contributions of the α events from other calcium nuclides, ^{42}Ca , ^{43}Ca , and ^{44}Ca , are less than 3 %, which is neglected in the data analysis.

The neutron energy spectra at the cathode position were measured using the EJ-309 liquid scintillator with unfolding method. Details of the EJ-309 liquid scintillator and the unfolding method are presented in our previous work [14]. The measured neutron energy spectra at each neutron energy (E_n) are shown in Fig. 2. One can see from Fig. 2 that in addition to the main-energy neutrons from the $^2\text{H}(d, n)^3\text{He}$ reaction, there are also low-energy neutrons, which is mainly from the $^2\text{H}(d, n + p)^2\text{H}$ reaction and the scattering from the walls. Interferences from the low-energy neutrons to the measurement events were corrected in Sec. III.

For each E_n , the four sample positions of the sample changer in the GIC were measured in turns. The fission events of the $^{238}\text{U}_3\text{O}_8\#1$ sample were measured simultaneously during the measurement to monitor the relative neutron fluence. The incident deuteron beam current was approximately 1.5 μA . The measurement duration for each neutron energy point was about 6 h. The EJ-309 liquid scintillator would run for ≈ 15.0 min per hour to obtain and check the neutron energy spectra.

III. DATA ANALYSIS

First, the α events from the $^{40}\text{Ca}(n, \alpha_0)^{37}\text{Ar}$ and $^{40}\text{Ca}(n, \alpha)^{37}\text{Ar}$ reactions were determined, respectively. Second, the fission events from the $^{238}\text{U}(n, f)$ reaction were determined. Finally, the cross sections for $^{40}\text{Ca}(n, \alpha_0)^{37}\text{Ar}$ and $^{40}\text{Ca}(n, \alpha)^{37}\text{Ar}$ reactions were obtained at each neutron energy.

A. Determination of the α events

The measured cathode-anode two-dimensional spectrum of the CaO sample in the forward direction at $E_n = 9.50$ MeV is shown in Fig. 3 as an example. Using the compound α source, energy calibration was performed and the valid area

TABLE I. Sample positions of the sample changer.

Sample position	Sample (01 side, forward)	Sample (02 side, backward)	Purpose
1	α source	α source	calibration of the GIC
2	$^{238}\text{U}_3\text{O}_8\#2$	Ta	absolute neutron fluence measurement
3	CaO#1	CaO#2	$^{40}\text{Ca}(n, \alpha_0)$ and $^{40}\text{Ca}(n, \alpha)$ measurement
4	Ta	Ta	background measurement
5	empty	empty	/

TABLE II. The data of the samples.

Samples	Mass thickness ($\mu\text{g}/\text{cm}^2$)	Isotopic enrichment	Diameter(cm)	Nucleus numbers	Backing
CaO#1	420.9	Natural (^{40}Ca 96.94%)	4.0	5.505×10^{19}	Ta
CaO#2	445.6	Natural (^{40}Ca 96.94%)	4.0	5.829×10^{19}	Ta
$^{238}\text{U}_3\text{O}_8\#1$	604.6	^{238}U 99.999%	4.5	2.064×10^{19}	Ta
$^{238}\text{U}_3\text{O}_8\#2$	600.8	^{238}U 99.999%	4.3	1.872×10^{19}	Ta

of the α events was located between the 0° curve and the 90° line corresponding to the emitting directions of the α particles perpendicular to and parallel to the cathode plate, respectively.

In the measured cathode-anode two-dimensional spectrum shown in Fig. 3, there are two types of nuclear reaction events. The first type is the events from the solid CaO sample located at the cathode plate, including the events from the $^{40}\text{Ca}(n, \alpha)^{37}\text{Ar}$ reaction and the $^{16}\text{O}(n, \alpha)^{13}\text{C}$ reaction. The second type is the events from the working gas in the GIC, including the $^{14}\text{N}(n, \alpha)^{11}\text{B}$ reaction from the nitrogen gas, $^{16}\text{O}(n, \alpha)^{13}\text{C}$ reaction from the oxygen gas, $^{\text{Nat}}\text{Xe}(n, \alpha)$ reaction from the xenon gas, and $^1\text{H}(n, el)$ reaction from the hydrogen gas, which could be eliminated after the background subtraction. The nitrogen and oxygen gases in the GIC are from the residual air during vacuum pumping.

After selecting the effective α events in the valid area (between the 0° curve and the 90° line in Fig. 3), the two-dimensional spectrum was projected onto the anode channel to get the anode spectrum. The anode spectra of the measured foreground events and the measured background events were obtained from the measured two-dimensional spectra of the CaO and Ta samples, respectively, as shown in Fig. 4. The anode spectra of the measured net events were obtained after background subtraction. The normalization factor for background subtraction is the ratio of the fission counts from $^{238}\text{U}_3\text{O}_8\#1$ sample in the measurements of the CaO sample to those in the measurements of the Ta sample. The α events

from the $^{40}\text{Ca}(n, \alpha)^{37}\text{Ar}$ and $^{40}\text{Ca}(n, \alpha)^{37}\text{Ar}$ reactions are determined separately.

1. $^{40}\text{Ca}(n, \alpha)^{37}\text{Ar}$ reaction

As shown in Fig. 4, the rightmost peak of the measured anode net spectra is the events from the $^{40}\text{Ca}(n, \alpha)^{37}\text{Ar}$ reaction, from which the counts of the α events (N_α) of the $^{40}\text{Ca}(n, \alpha)^{37}\text{Ar}$ reaction within the thresholds can be obtained. The detection efficiency of the α events (ε_α) for the $^{40}\text{Ca}(n, \alpha)^{37}\text{Ar}$ reaction is determined using Monte Carlo simulation. The angular distributions of the α particles for this reaction were calculated utilizing TALYS-1.9 code [15] and the stopping powers were calculated with SRIM-2013 code [16]. The simulated anode spectrum of the $^{40}\text{Ca}(n, \alpha)^{37}\text{Ar}$ reaction at $E_n = 9.50$ MeV is also shown in Fig. 4. The values of ε_α for the $^{40}\text{Ca}(n, \alpha)^{37}\text{Ar}$ reaction are from 74.3%–78.3% for forward measurements and from 72.6%–84.1% for backward measurements.

2. $^{40}\text{Ca}(n, \alpha)^{37}\text{Ar}$ reaction

The measured net events for the $^{40}\text{Ca}(n, \alpha)^{37}\text{Ar}$ reaction are comprised of three parts: the α events from the $^{40}\text{Ca}(n, \alpha)^{37}\text{Ar}$ reaction induced by the main-energy neutrons, the α events from the $^{16}\text{O}(n, \alpha)^{13}\text{C}$ reaction of the CaO sample induced by the main-energy neutrons, and the α events from the $^{40}\text{Ca}(n, \alpha)^{37}\text{Ar}$ reaction induced by the low-energy neutrons. The $^{16}\text{O}(n, \alpha)^{13}\text{C}$ reaction induced by the

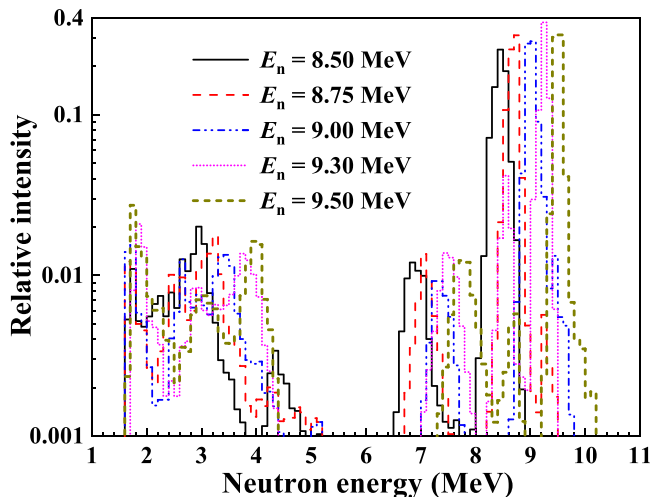


FIG. 2. The neutron energy spectra measured using the EJ-309 liquid scintillator.

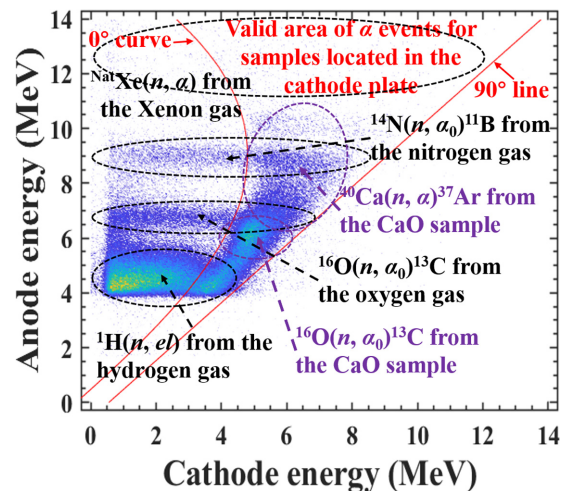


FIG. 3. The measured cathode-anode two-dimensional spectrum of the CaO sample in the forward direction at $E_n = 9.50$ MeV.

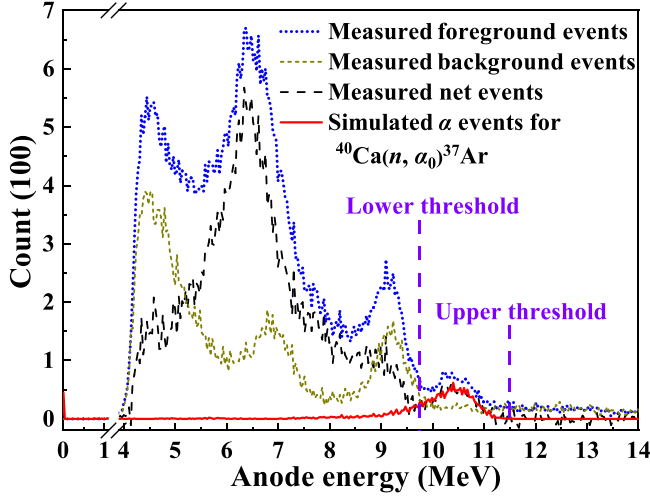


FIG. 4. The measured anode spectra of the net events, foreground events, and background events, and the simulated anode spectra of the α events from the $^{40}\text{Ca}(n, \alpha)^{37}\text{Ar}$ reaction in the forward direction at $E_n = 9.50$ MeV.

low-energy neutrons is neglected, because the energies of these α particles are below the measurement threshold.

The anode spectra of the above three parts were simulated using Monte Carlo method, in which the double differential cross sections for different reactions were calculated with TALYS-1.9 code [15]. In the simulation of the $^{40}\text{Ca}(n, \alpha)^{37}\text{Ar}$ reaction induced by the low-energy neutrons, the neutron energy spectra measured with the EJ-309 liquid scintillator (Fig. 2) were used.

Figure 5 shows the measured and simulated anode spectra for $E_n = 9.50$ MeV in the forward direction. The consistency between the measured anode spectra of net events and

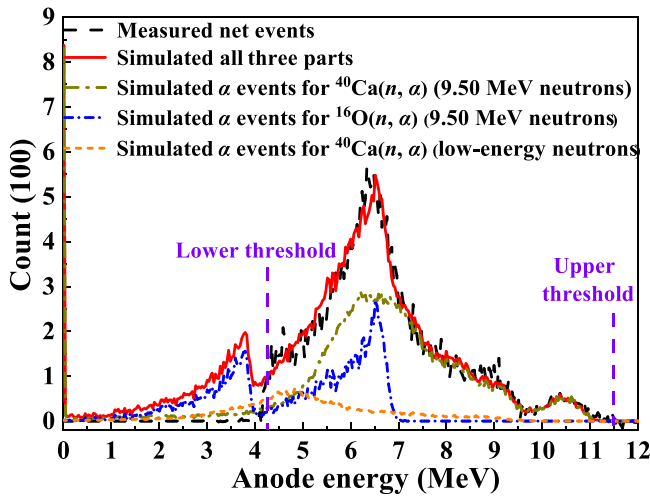


FIG. 5. The measured anode spectrum of the net events in the forward direction for $E_n = 9.50$ MeV. The simulated anode spectrum of the α events from the $^{40}\text{Ca}(n, \alpha)^{37}\text{Ar}$ reaction induced by 9.50 MeV neutrons, from the $^{16}\text{O}(n, \alpha)^{13}\text{C}$ reaction induced by the 9.50 MeV neutrons and from the $^{40}\text{Ca}(n, \alpha)^{37}\text{Ar}$ reaction induced by the low-energy neutrons.

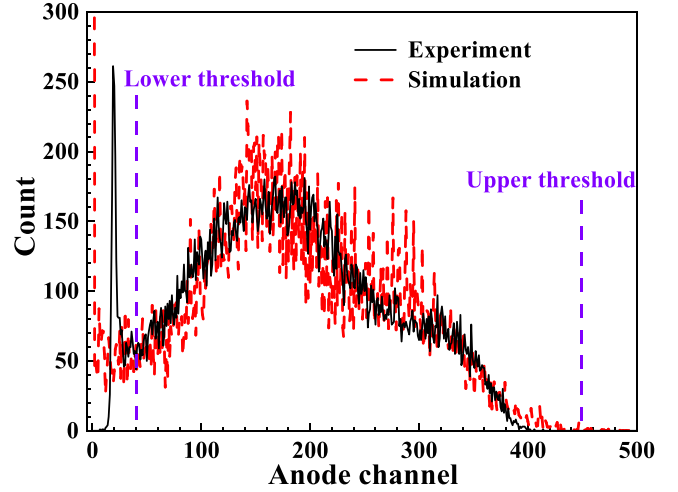


FIG. 6. The measured and simulated anode spectra from the $^{238}\text{U}(n, f)$ reaction of $^{238}\text{U}_3\text{O}_8\#2$ at $E_n = 9.00$ MeV.

the simulated anode spectra of all the three parts indicates the reliability of the simulations. Some α events from the $^{16}\text{O}(n, \alpha)^{13}\text{C}$ reaction and from the $^{40}\text{Ca}(n, \alpha)^{37}\text{Ar}$ reaction induced by the low-energy neutrons are located within the thresholds. After the correction of the above interferences by the simulation, the counts of the α events (N_α) for the $^{40}\text{Ca}(n, \alpha)^{37}\text{Ar}$ reaction are determined. The detection efficiency of the α events (ε_α) for the $^{40}\text{Ca}(n, \alpha)^{37}\text{Ar}$ reaction is also determined using the simulation. The values of ε_α for the $^{40}\text{Ca}(n, \alpha)^{37}\text{Ar}$ reaction are from 85.0%–91.0% for the forward measurement and from 73.8%–80.5% for the backward measurement. The measured and simulated anode spectra for the forward and backward directions for the five neutron energies are presented in the Appendix.

TABLE III. Sources of the uncertainty and their magnitudes.

Source	Magnitude (%)	
	$^{40}\text{Ca}(n, \alpha)^{37}\text{Ar}$	$^{40}\text{Ca}(n, \alpha)^{37}\text{Ar}$
σ_f	1.4–1.5 ^{a, b}	1.4–1.5 ^{a, b}
$N_{238\text{U}}$	1.0 ^{a, b}	1.0 ^{a, b}
N_{Ca}	1.0 ^{a, b}	1.0 ^{a, b}
N_α	1.7–2.8 ^a , 1.6–3.0 ^b	3.7–8.1 ^a , 2.8–4.5 ^b
ε_α	4.3–5.1 ^a , 3.2–4.3 ^b	3.3–5.0 ^a , 6.5–9.0 ^b
N_f	0.52–0.62 ^{a, b}	0.52–0.62 ^{a, b}
ε_f	0.94–1.2 ^{a, b}	0.94–1.2 ^{a, b}
ρ_{main}	1.5–2.0 ^{a, b}	1.5–2.0 ^{a, b}
R	0.35–0.41 ^{a, b}	0.35–0.41 ^{a, b}
K	1.0 ^{a, b}	1.0 ^{a, b}
E_n	0.7–1.4 ^{a, b}	0.7–1.4 ^{a, b}
σ_α	5.9–6.6 ^a , 5.0–6.8 ^b , 5.6–6.4 ^c	6.4–9.8 ^a , 8.3–9.9 ^b , 7.2–9.7 ^c

^aFor forward cross sections.

^bFor backward cross sections.

^cFor total cross sections.

TABLE IV. Measured cross sections and forward to backward ratios in the laboratory reference system for the $^{40}\text{Ca}(n, \alpha_0)^{37}\text{Ar}$ and $^{40}\text{Ca}(n, \alpha)^{37}\text{Ar}$ reactions.

E_n (MeV)	Cross sections (mb)		Forward/backward ratio	
	$^{40}\text{Ca}(n, \alpha_0)^{37}\text{Ar}$	$^{40}\text{Ca}(n, \alpha)^{37}\text{Ar}$	$^{40}\text{Ca}(n, \alpha_0)^{37}\text{Ar}$	$^{40}\text{Ca}(n, \alpha)^{37}\text{Ar}$
8.50 ± 0.12	22.8 ± 1.5	174.4 ± 12.6	1.03 ± 0.07	1.31 ± 0.10
8.75 ± 0.09	19.5 ± 1.5	173.2 ± 16.7	1.08 ± 0.08	1.28 ± 0.12
9.00 ± 0.09	16.5 ± 1.0	168.9 ± 15.9	1.13 ± 0.07	1.38 ± 0.13
9.30 ± 0.07	14.4 ± 0.9	167.9 ± 15.8	1.19 ± 0.08	1.38 ± 0.13
9.50 ± 0.07	12.5 ± 0.7	163.3 ± 14.5	1.34 ± 0.08	1.40 ± 0.12

B. Determination of the fission events

The fission events from the $^{238}\text{U}_3\text{O}_8\#2$ sample set at the position No. 2 of the sample changer were used to determine the absolute neutron fluence. A typical anode spectrum of the $^{238}\text{U}(n, f)$ reaction is shown in Fig. 6 as an example. The lower threshold is set to reject the α particles from the decay of the ^{238}U . The counts of the fission events (N_f) are the sum of the measured anode spectra within the lower and upper thresholds. The detection efficiency of the fission events (ε_f) is calculated using Monte Carlo simulation, details of which are described in Ref. [13]. As shown in Fig. 6, the simulated anode spectrum of the $^{238}\text{U}(n, f)$ reaction is consistent with the measured one. The values of ε_f are from 88.1%–90.2%.

The ratio of the fission events induced by the main-energy neutrons to the fission events induced by all neutrons (ρ_{main}) could be determined by

$$\rho_{\text{main}} = \frac{\sum_{E_i \in \text{main-energy neutrons}} H_{E_i} \cdot \sigma_f^{E_i}}{\sum_{E_i \in \text{all neutrons}} H_{E_i} \cdot \sigma_f^{E_i}}, \quad (1)$$

where H_{E_i} is the relative intensity of the measured neutron energy spectra (Fig. 2) at the neutron energy E_i , $\sigma_f^{E_i}$ is the standard cross section of the $^{238}\text{U}(n, f)$ reaction at the neutron energy E_i [17]. The values of ρ_{main} in the present work are from 0.803–0.836.

C. Calculation of the cross sections

The forward and backward cross sections of the (n, α_0) and (n, α) reactions (σ_α) can be calculated with

$$\sigma_\alpha = \sigma_f \cdot \frac{N_{238\text{U}} \cdot N_\alpha \cdot \varepsilon_f \cdot R}{N_{40\text{Ca}} \cdot N_f \cdot \varepsilon_\alpha \cdot \rho_{\text{main}}} K, \quad (2)$$

where σ_f is the standard cross section of the $^{238}\text{U}(n, f)$ reaction at the specific neutron energy [17]. $N_{238\text{U}}$ and $N_{40\text{Ca}}$ are the numbers of the ^{238}U and ^{40}Ca nucleus in the $^{238}\text{U}_3\text{O}_8\#2$ and CaO samples, separately. N_α is the count of the α events from $^{40}\text{Ca}(n, \alpha_0)^{37}\text{Ar}$ or $^{40}\text{Ca}(n, \alpha)^{37}\text{Ar}$ reactions. ε_α is the detection efficiency of the α events for $^{40}\text{Ca}(n, \alpha_0)^{37}\text{Ar}$ or $^{40}\text{Ca}(n, \alpha)^{37}\text{Ar}$ reactions. N_f is the counts of the fission events. ε_f is the detection efficiency of the fission events. ρ_{main} is the ratio of the fission events induced by the main-energy neutrons to the fission events induced by all neutrons calculated from Eq. (1). K is the ratio of the average neutron fluence in the area of the CaO sample to that of the $^{238}\text{U}_3\text{O}_8\#2$ sample in the sample changer, which is obtained by the Monte Carlo simulation. The values of K are from 0.99–1.00 because

the positions and the diameters of the CaO samples and the $^{238}\text{U}_3\text{O}_8\#2$ sample are almost the same. R is the ratio of the fission counts from the $^{238}\text{U}_3\text{O}_8\#1$ sample glued on the fission cathode during the CaO measurement to that during the $^{238}\text{U}_3\text{O}_8\#2$ measurement for normalization.

IV. EXPERIMENTAL RESULTS

The forward and backward cross sections of the $^{40}\text{Ca}(n, \alpha_0)^{37}\text{Ar}$ and $^{40}\text{Ca}(n, \alpha)^{37}\text{Ar}$ reactions are calcu-

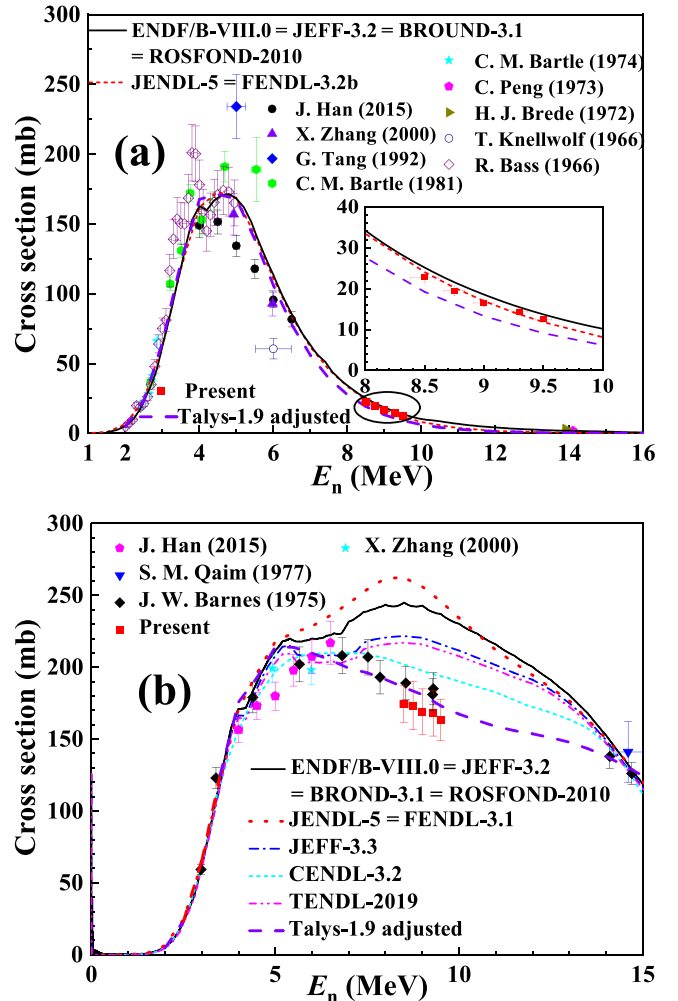


FIG. 7. The cross sections of the (a) $^{40}\text{Ca}(n, \alpha_0)^{37}\text{Ar}$ and (b) $^{40}\text{Ca}(n, \alpha)^{37}\text{Ar}$ reactions.

TABLE V. Adjusted input parameters of TALYS-1.9 [13].

Keywords	Parameter
ldmodel	4
maxlevelsbin	a 6
Tljadjust	a 1.6 0

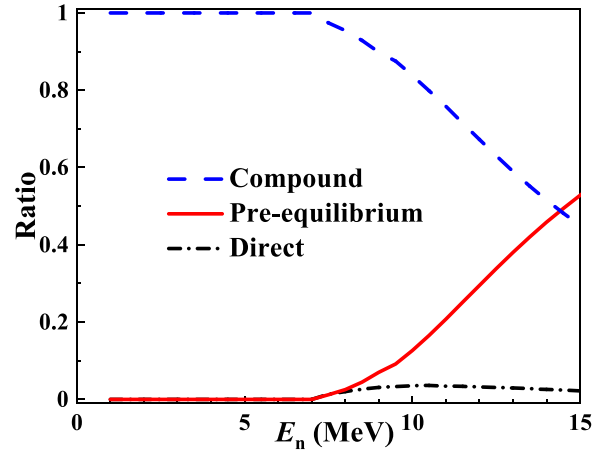
lated using Eq. (2). Sources of the uncertainty and their magnitudes are presented in Table III. The total (n, α_0) and (n, α) cross sections are obtained by adding up the forward and backward cross sections. In addition to the cross sections, the forward to backward ratios for the $^{40}\text{Ca}(n, \alpha_0)^{37}\text{Ar}$ and $^{40}\text{Ca}(n, \alpha)^{37}\text{Ar}$ reactions in the laboratory reference system are also acquired. Data of measurement results are shown in Table IV.

As Table IV shows, the forward to backward ratios of the $^{40}\text{Ca}(n, \alpha_0)^{37}\text{Ar}$ reaction in the laboratory reference system gradually increase with the increase of neutron energy. The forward to backward ratios of the $^{40}\text{Ca}(n, \alpha)^{37}\text{Ar}$ reaction measured in the present work are from 1.28–1.40, obviously bigger than 1.10. Calculations show that for $E_n < 9.50$ MeV, the forward to backward ratios of the $^{40}\text{Ca}(n, \alpha)^{37}\text{Ar}$ reaction in the laboratory reference system should be less than 1.10 assuming that the angular distributions of emitted α particles are isotropic in the center-of-mass system. Our work indicates that the angular distributions of the emitted α particles in the center-of-mass system from the $^{40}\text{Ca}(n, \alpha)^{37}\text{Ar}$ reaction are forward peaked and the statistical mechanism of the compound nucleus is not entirely applicable for the $^{40}\text{Ca}(n, \alpha)^{37}\text{Ar}$ reaction in the 8.50–9.50 MeV region.

Present results are compared with existing experimental data from the EXFOR library [7] and evaluation data from the ENDF/B-VIII.0 [8], JENDL-5 [9], JEFF-3.3 [10], CENDL-3.2 [11], ROSFOND-2010 [18], and TENDL-2019 [12] libraries, as shown in Fig. 7. For the $^{40}\text{Ca}(n, \alpha_0)^{37}\text{Ar}$ reaction, there is no measurement in the 8.00–10.00 MeV neutron energy region. The present cross sections agree with the ENDF/B-VIII.0 and JENDL-5 libraries. For the $^{40}\text{Ca}(n, \alpha)^{37}\text{Ar}$ reaction, the present cross sections agree with the measurement data of Barnes *et al.* [3] within uncertainties. Both our and Barnes's measurement data are lower than all existing evaluation data in the 8.00–10.00 MeV

TABLE VI. Calculated cross sections and forward to backward ratios in the laboratory reference system for the $^{40}\text{Ca}(n, \alpha_0)^{37}\text{Ar}$ and $^{40}\text{Ca}(n, \alpha)^{37}\text{Ar}$ reactions.

E_n (MeV)	Cross sections (mb)		Forward/backward ratio	
	$^{40}\text{Ca}(n, \alpha_0)^{37}\text{Ar}$	$^{40}\text{Ca}(n, \alpha)^{37}\text{Ar}$	$^{40}\text{Ca}(n, \alpha_0)^{37}\text{Ar}$	$^{40}\text{Ca}(n, \alpha)^{37}\text{Ar}$
8.50	19.3	186.1	1.08	1.17
8.75	16.0	185.6	1.08	1.18
9.00	13.3	180.9	1.08	1.21
9.30	11.0	180.4	1.08	1.23
9.50	9.2	173.1	1.08	1.24

FIG. 8. The ratio of the direct, preequilibrium and compound components of the $^{40}\text{Ca}(n, \alpha)^{37}\text{Ar}$ cross sections calculated using the TALYS-1.9 code with the adjusted parameters.

neutron energy region. The present results are helpful in obtaining precise excitation function of the $^{40}\text{Ca}(n, \alpha)^{37}\text{Ar}$ reaction.

V. THEORETICAL ANALYSIS AND DISCUSSIONS

Cross sections of the $^{40}\text{Ca}(n, \alpha_0)^{37}\text{Ar}$ and $^{40}\text{Ca}(n, \alpha)^{37}\text{Ar}$ reactions were calculated using TALYS-1.9 code [15]. To agree better with the present results, three input parameters of the level density model were adjusted, as listed in Table V. The Skyrme-Hartree-Fock-Bogolyubov level densities was used in the calculation [15]. The calculated cross sections agree in general with the present measurement results as presented in Fig. 7. The calculated forward to backward ratios in the laboratory reference system for the $^{40}\text{Ca}(n, \alpha_0)^{37}\text{Ar}$ and $^{40}\text{Ca}(n, \alpha)^{37}\text{Ar}$ reactions are presented in Table VI, which are consistent with the measurement data listed in Table IV.

From calculations, the direct, preequilibrium and compound components of the $^{40}\text{Ca}(n, \alpha)^{37}\text{Ar}$ reaction were obtained as a function of the incident neutron energy. As shown in Fig. 8, the ratios of the compound component are nearly 100% when E_n is below 7 MeV and they decrease from 100%–45% as E_n increases from 7–15 MeV. The ratios

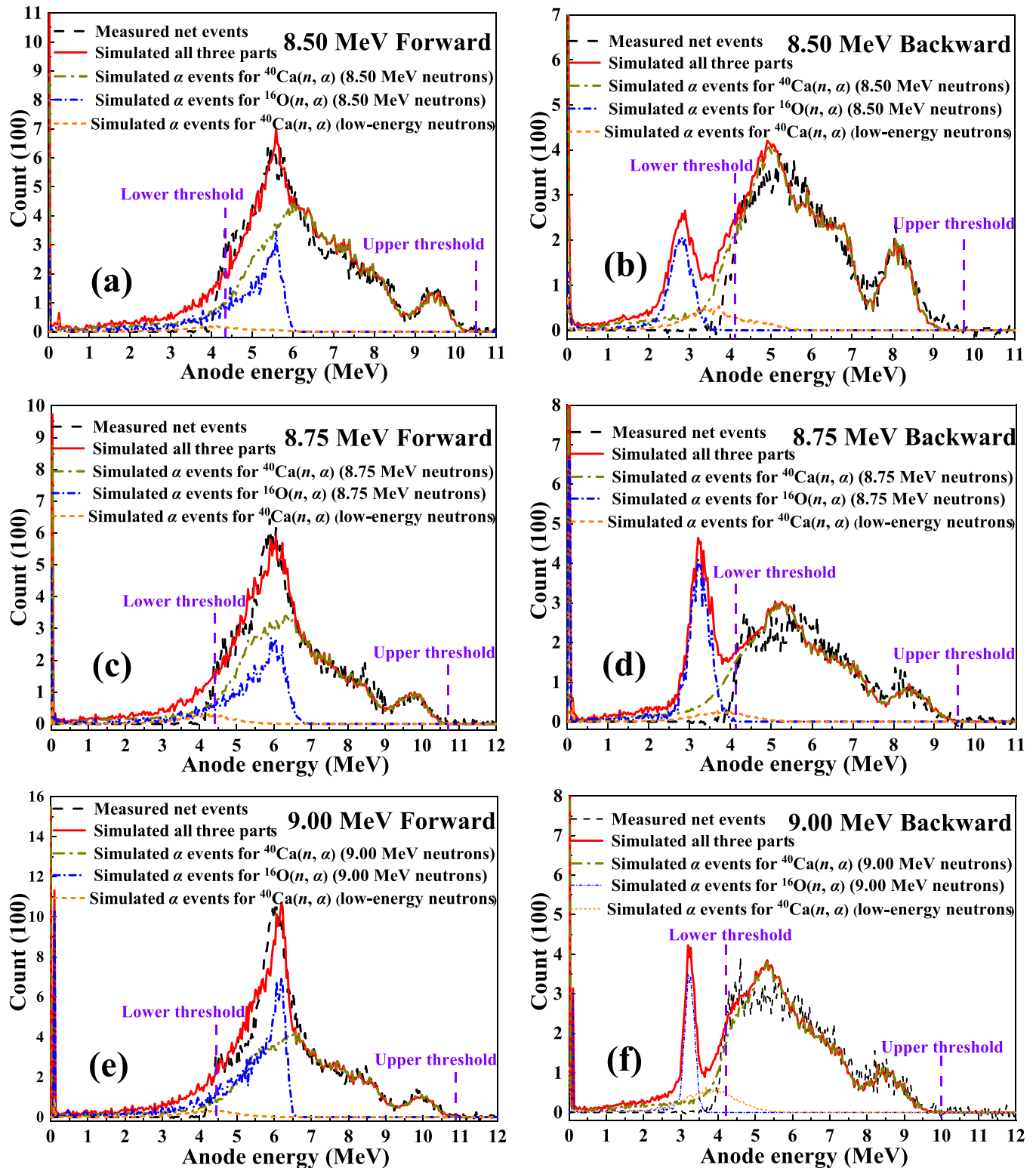


FIG. 9. The measured and simulated anode spectra for the forward and backward directions, respectively, at neutron energies of (a)–(b) 8.50 MeV, (c)–(d) 8.75 MeV, and (e)–(f) 9.00 MeV.

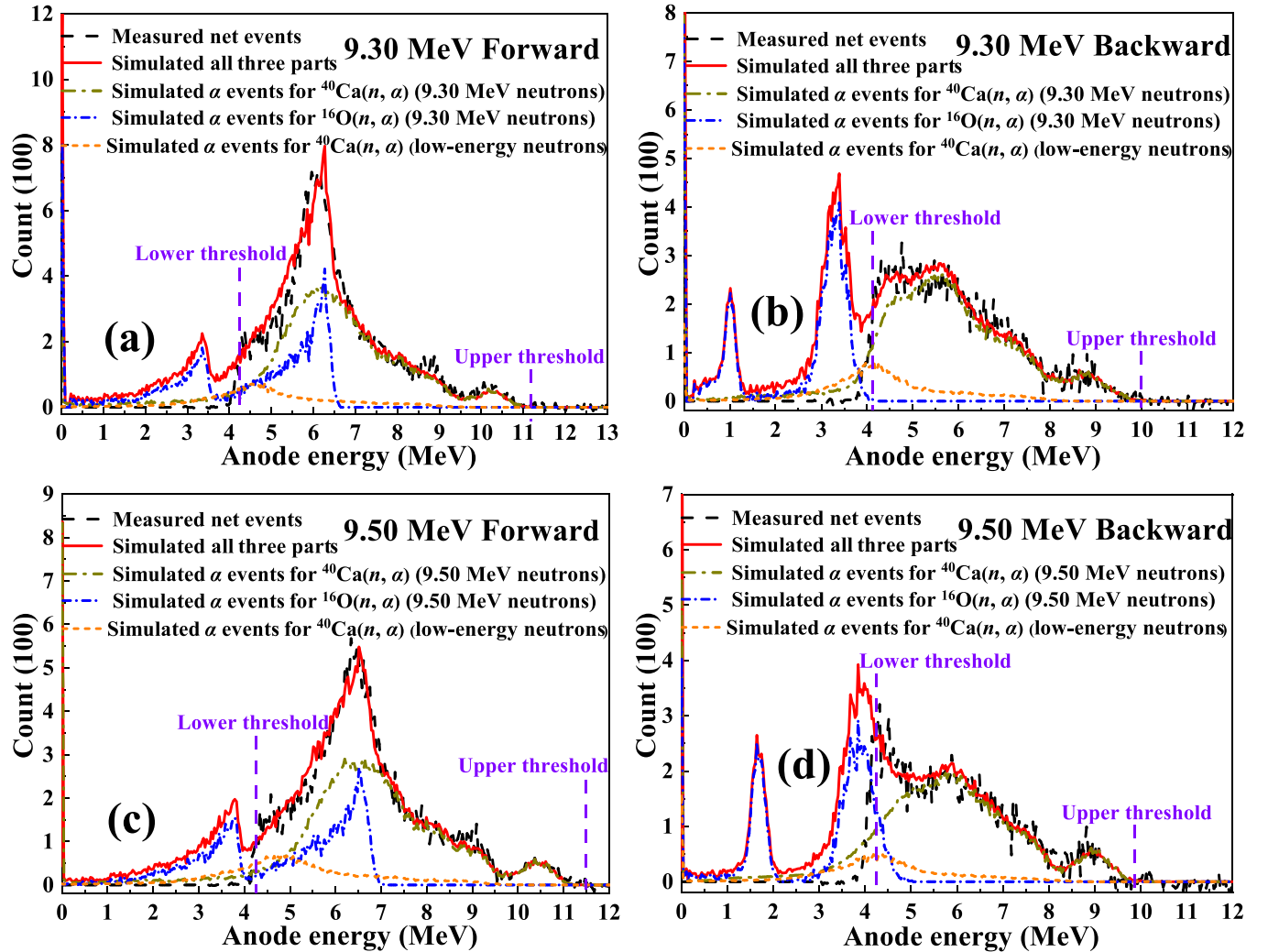


FIG. 10. The measured and simulated anode spectra for the forward and backward directions, respectively, at neutron energies of (a)–(b) 9.30 MeV and (c)–(d) 9.50 MeV.

of the preequilibrium component increase from 0 to 53% as E_n increases from 7–15 MeV and the contribution of the preequilibrium mechanism is bigger than that of the compound mechanism as E_n is higher than 14.4 MeV. The direct mechanism gradually come into effect as E_n increases from 7–15 MeV with the ratio less than 4%. From 8.50–9.50 MeV, the ratios of the direct and preequilibrium components are increase from 2.6%–3.3% and from 4.4%–9.2%, respectively. The contribution of the direct and preequilibrium mechanisms in the 8.50–9.50 MeV region is non-negligible although the compound mechanism predominates this reaction, which is consistent with our present measurement results of forward to backward ratios.

VI. CONCLUSIONS

Cross sections of the $^{40}\text{Ca}(n, \alpha_0)^{37}\text{Ar}$ and $^{40}\text{Ca}(n, \alpha)^{37}\text{Ar}$ reactions were measured at five neutron energies from 8.50–9.50 MeV. For the $^{40}\text{Ca}(n, \alpha_0)^{37}\text{Ar}$

reaction, the present data are in good agreement with the data in ENDF/B-VIII.0 and JENDL-5 libraries. For the $^{40}\text{Ca}(n, \alpha)^{37}\text{Ar}$ reaction, the present data agree with the measurement data of Barnes *et al.* within measurement uncertainties. The data of both present and Barnes's measurements in the 8.50–9.50 MeV region are lower than those of all existing evaluations. The present data are helpful to constrain the excitation function of the $^{40}\text{Ca}(n, \alpha)^{37}\text{Ar}$ reaction.

The calculated cross sections using TALYS-1.9 code with the adjusted input parameters of the level density model agree with the present measurement results. Calculations show that in the 8.50–9.50 MeV region the compound mechanism predominates the $^{40}\text{Ca}(n, \alpha)^{37}\text{Ar}$ reaction and from 8.50–9.50 MeV the ratios of the direct and preequilibrium components increase from 2.6%–3.3% and from 4.4%–9.2%, respectively. The contribution of the direct and preequilibrium mechanism is non-negligible, which is consistent with the present measurement results of the forward to backward ratios.

ACKNOWLEDGMENTS

The anonymous reviewer is acknowledged for their comments that improved the quality of this paper. The authors are indebted to the operation crew of the Beijing HI-13 Tandem Accelerator of China Institute of Atomic Energy. This work was financially supported by the National Natural Science Foundation of China (Grant No. 12075008) and the Key Laboratory of Nuclear Data foundation (6142A08200103).

APPENDIX

Figure 9 shows the measured and simulated anode spectra for the forward and backward directions respectively at neutron energies of 8.50 MeV [Figs. 9(a), 9(b)], 8.75 MeV [Figs. 9(c), 9(d)], and 9.00 MeV [Figs. 9(e), 9(f)]. Figure 10 shows the measured and simulated anode spectra for the forward and backward directions, respectively, at neutron energies of 9.30 MeV [Figs. 10(a), 10(b)] and 9.50 MeV [Figs. 10(c), 10(d)].

-
- [1] H. Bai, H. Jiang, Y. Lu, Z. Cui, J. Chen, G. Zhang, Yu. M. Gledenov, M. V. Sedysheva, G. Khuukhenkhuu, X. Ruan *et al.*, *Phys. Rev. C* **99**, 024619 (2019).
- [2] S. M. Qaim, A. Rusheed, G. Stöcklin, and R. Wölflé, *Int. J. Appl. Radiat. and Isot.* **28**, 6 (1977).
- [3] J. W. Barnes, B. P. Bayhurst, B. H. Erkkilä, J. S. Gilmore, Nelson Jarmie, and R. J. Prestwood, *J. Inorg. Nucl. Chem.* **37**, 2 (1975).
- [4] C. M. Egnatuk, J. Lowrey, S. R. Biegalski, T. Bowyer, D. Haas, J. Orrell, V. Woods, and M. Keillor, *J. Radioanal. Nucl. Chem.* **291**, 257 (2012).
- [5] X. Zhang, Z. Chen, Y. Chen, G. Tang, G. Zhang, J. Chen, Yu. M. Gledenov, and G. Khuukhenkhuu, *Nucl. Sci. Eng.* **134**, 89 (2000).
- [6] J. Han, J. Liu, X. Liu, X. Fan, Z. Wang, J. Chen, G. Zhang, Yu. M. Gledenov, M. V. Sedysheva, L. Krupa, G. Khuukhenkhuu, and P. J. Szalanski, *Eur. Phys. J. A* **51**, 12 (2015).
- [7] Experimental Nuclear Reaction Data (EXFOR), <https://www.nndc.bnl.gov/exfor>.
- [8] D. A. Brown, M. B. Chadwick, R. Capote, A. C. Kahler, A. Trkov, M. W. Herman, A. A. Sonzogni, Y. Danon, A. D. Carlson, M. Dunn, D. L. Smith *et al.*, *Nucl. Data Sheets* **148**, 1 (2018).
- [9] O. Iwamoto, N. Iwamoto, K. Shibata, A. Ichihara, S. Kunieda, F. Minato, and S. Nakayama, *EPJ Web Conf.* **239**, 09002 (2020).
- [10] JEFF-3.3, <https://www.oecd-nea.org/dbdata/jeff/jeff33/index.html>
- [11] CENDL-3.2, <http://www.nuclear.csdb.cn/pingjia.html>
- [12] A. J. Koning, D. Rochman, J. Sublet, N. Dzysiuk, M. Fleming, and S. van der Marck, *Nucl. Data Sheets* **155**, 1 (2019).
- [13] H. Jiang, Z. Cui, Y. Hu, J. Liu, J. Chen, G. Zhang, Yu. M. Gledenov, E. Sansarbayar, G. Khuukhenkhuu, and L. Krupa, *Chin. Phys. C* **44**, 114102 (2020).
- [14] H. Bai, Z. Wang, L. Zhang, H. Jiang, Y. Lu, J. Chen, and G. Zhang, *Nucl. Instrum. Meth. Phys. Res. A* **886**, 109 (2018).
- [15] A. J. Koning, S. Hilaire, and S. Goriely, TALYS-1.9 (2017), <http://www.TALYS.eu/>
- [16] J. F. Ziegler, SRIM-2013, <http://www.srim.org/#SRIM>
- [17] A. D. Carlson, V. G. Pronyaev, R. Capote, G. M. Hale, Z. P. Chen, I. Duran, F. J. Hamsch, S. Kunieda, W. Mannhart, B. Marcinkevicius *et al.*, *Nucl. Data Sheets* **148**, 143 (2018).
- [18] S. V. Zabrodskaia, A. V. Ignatyuk, V. N. Koshcheev, V. N. Manochin, M. N. Nikolaev, and V. G. Pronyaev, *Ser. Nucl. Const.* **1-2**, 3 (2007).